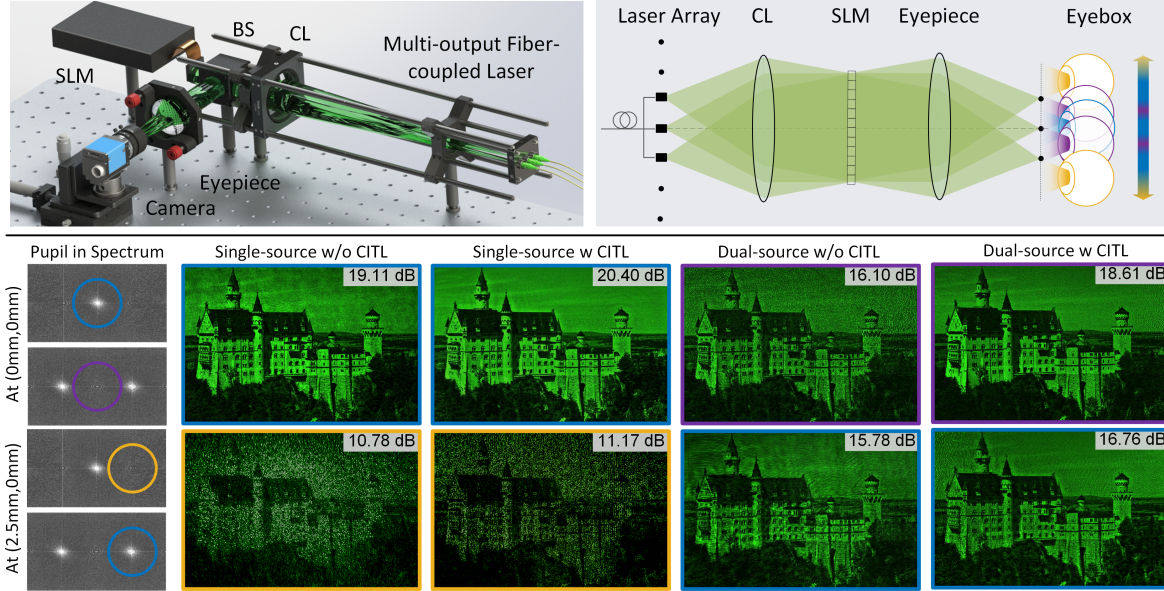


# Multi-illumination-interfered Neural Holography with Expanded Eyebox

Xinxing Xia , Pengfei Mi, Yiqing Tao, Xiangyu Meng , Wenbin Zhou , Yingjie Yu, and Yifan Peng 



**Fig. 1:** **Top-left:** Conceptual holographic display. Fiber laser outputs pass through BS, LP, and CL to illuminate the SLM. **Top-right:** Eyebox expansion schematic. Multi-angle illumination creates adjacent viewpoints on the eyepiece's focal plane. Pupil shifts align viewpoints at center (blue), edge (yellow), or both simultaneously (purple). **Bottom:** Experimental single vs. dual illumination, with/without CITL. First row: Pupil centered at (0 mm, 0 mm). Dual illumination achieves clarity even at single-source spectrum edges. Second row: Single illumination shows limited quality. Dual maintains fidelity within combined spectral range, expanding eyebox. (Dual-light configuration simplified in experiments.)

**Abstract**— Holography has immense potential for near-eye displays in virtual and augmented reality (VR/AR), providing natural 3D depth cues through wavefront reconstruction. However, balancing the field of view (FOV) with the eyebox remains challenging, constrained by the étendue limitation. Additionally, holographic image quality is often compromised due to differences between actual wave propagation and simulation models. This study addresses these by expanding the eyebox via multi-angle illumination, and enhancing image quality with end-to-end pupil-aware hologram optimization. Further, energy efficiency is improved by incorporating higher-order diffractions and pupil constraints. We explore a Pupil-HOGD algorithm for multi-angle illumination and validate it with a dual-angle holographic display prototype. Integrated with camera calibration and tracked eye position, the developed *Pupil-HOGD* algorithm improves image quality and expands the eyebox by 50% horizontally. We envision this approach extends the space-bandwidth product (SBP) of holographic displays, enabling broader applications in immersive, high-quality visual computing.

**Index Terms**—Holographic display, Multi-illumination, Eyebox, Camera-in-the-loop calibration

## 1 INTRODUCTION

- Xinxing Xia, Pengfei Mi, Yiqing Tao, and Yingjie Yu are with the School of Mechatronic Engineering and Automation, Shanghai University, Shanghai 200444, China (E-mail: [xiainxing@shu.edu.cn](mailto:xiainxing@shu.edu.cn); [mi\\_pengfei@foxmail.com](mailto:mi_pengfei@foxmail.com); [tyq211218@126.com](mailto:tyq211218@126.com); [yingjieyu@staff.shu.edu.cn](mailto:yingjieyu@staff.shu.edu.cn)). Xinxing Xia is also with Shangda General Intelligent Robotics Research Institute, Shanghai, China.
- Xiangyu Meng, Wenbin Zhou, and Yifan Peng are with the Department of Electrical and Electronic Engineering, The University of Hong Kong, Hong Kong SAR, China (E-mail: [mengxy22@connect.hku.hk](mailto:mengxy22@connect.hku.hk); [zhouwb@connect.hku.hk](mailto:zhouwb@connect.hku.hk); [evanpeng@hku.hk](mailto:evanpeng@hku.hk)).
- Corresponding authors: Yifan Peng and Xinxing Xia.

Manuscript received xx xxx. 201x; accepted xx xxx. 201x. Date of Publication xx xxx. 201x; date of current version xx xxx. 201x. For information on obtaining reprints of this article, please send e-mail to: [reprints@ieee.org](mailto:reprints@ieee.org). Digital Object Identifier: [xx.xxxx/TVCG.201x.xxxxxxx](https://doi.org/10.1109/TVCG.201x.xxxxxxx)

Near-eye display systems designed for virtual reality (VR) and augmented reality (AR) have received significant attention [28]. Traditional binocular parallax displays frequently induce the vergence accommodation conflict (VAC), degrading the visual experience [17]. While emerging technologies such as retinal projection/Maxwellian-view, multi-focal, varifocal, light field, and holographic displays [38] have been developed to mitigate VAC, achieving natural depth cues within compact form factors remains an unresolved challenge. Holographic near-eye displays stand out by offering full 3D capabilities with inherent optical aberration correction [8, 22, 34], yet face fundamental limitations in their space-bandwidth product (SBP) [23, 27].

Current holographic systems face a critical trade-off between eyebox size and FOV due to SBP constraints. Existing eyebox expansion strategies exhibit inherent limitations: exit-pupil replication degrades image quality through diffraction artifacts [9, 31], mechanical scanning introduces system complexity and latency [20, 41], while multi-angle illumination induces image aliasing without pupil-adaptive compensa-

tion [4]. Although advances in computer-generated holography (CGH) algorithms (e.g., iterative optimization and deep learning) and hardware calibration techniques (e.g., camera-in-the-loop optimization) have improved visual fidelity, their integration with eyebox expansion mechanisms remains underexplored, leading to compromised performance in practical implementations.

To address these limitations, we present a pupil-adaptive holographic display system integrating three key innovations: (1) a multi-angle illumination configuration for SBP enhancement, (2) a pupil-in-the-loop (PITL) optimization algorithm, and (3) a rotational angular spectrum strategy for aliasing suppression. Central challenges resolved in this work include maintaining image fidelity under dynamic pupil variations, eliminating higher-order diffraction artifacts in multi-angle systems, and preserving resolution during eyebox expansion.

This study introduces the *Pupil-HOGD* hologram optimization algorithm with angular spectrum rotation and spatial domain shifting techniques to mitigate diffraction artifacts and aliasing distortions. Integrated with off-the-shelf eye-tracking, the proposed method dynamically adjusts angular spectrum rotation and spatial shifts based on real-time pupil measurements, thereby reducing image degradation caused by multi-angle illumination. Additionally, the *Pupil-HOGD* algorithm tackles higher-order diffraction effects by employing constrained gradient descent optimization, specifically designed to accommodate pupil conditions. Our main technical contributions include:

- We propose a multi-angle illumination scheme integrated with the pupil-in-the-loop optimization framework to enhance the space-bandwidth product and expand the eyebox of holographic displays. We effectively mitigate image aliasing caused by simultaneous multi-angle illumination while adapting to pupil size and positional variations.
- We explore a hologram optimization algorithm, dubbed Pupil-HOGD, that addresses higher-order diffraction artifacts and preserves image quality under varying pupil conditions. This overcomes the persistent challenge of diffraction-induced distortions in holographic displays through advanced phase-modulation optimization, ensuring consistent visual fidelity across expanded eyebox ranges.
- We establish an experimental framework, enabling eyebox expansion without compromising field-of-view or image resolution. Validated by a dual-angle illumination prototype, our design achieves 50% horizontal eyebox expansion while maintaining high image quality, demonstrating a practical advancement in holographic displays.

## 2 RELATED WORK

**Eyebox-expanded Holographic Displays.** Holographic near-eye displays are fundamentally constrained by the space-bandwidth product (SBP) [23, 27], resulting in an inherent trade-off between eyebox and FOV. Existing approaches addressing this limitation can be categorized as static pupil replication and dynamic pupil steering. Static approaches, such as lens array-based holographic optical elements (HOEs) coupled with higher-order diffraction simulation presented by Park et al. [9, 31], enable 3D eyebox expansion at the expense of reduced diffraction efficiency. Dynamic strategies, employing MEMS-based scanning systems, offer enhanced adaptability. Jang et al. [20] implemented real-time pupil steering via synchronized MEMS mirrors and HOE gratings, whereas Xia et al. [41] realized 2D pupil translation through active beam manipulation. However, these dynamic methods introduce an increased system complexity and potential temporal distortions during rapid eye movements.

**Holographic Displays via Multi-source Illumination.** Multi-angle illumination strategies have emerged as promising alternatives to conventional pupil expansion techniques, leveraging angular diversity rather than spatial multiplexing. Temporal multiplexing approaches like Wang et al. [37] enable virtual SLM stitching through synchronized beam deflectors, though requiring precise timing control. Spatial multiplexing methods address SLM diffraction limits directly. Specifically,

Jo et al. [21] used discrete laser diodes for angular sampling but faced coherence management challenges, while Lee et al. [43] demonstrated coherent multi-illumination holography requiring sub-micron alignment precision. Incoherent dual-SLM configurations, such as those explored by Meta Reality Labs, prioritize speckle mitigation, yielding a very limited increase in eyebox [24]. The latest advancement by Chao et al. [5] introduces an additional amplitude-only SLM on the Fourier plane with multisource illumination, enabling at least  $2\times$  eyebox expansion, but achieves suboptimal image quality due to the lack of eye tracking. Crucially, existing multi-angle systems typically lack dynamic pupil adaptation mechanisms, resulting in aliasing artifacts during eye rotations.

**Learning-driven Hologram Generation.** Modern hologram synthesis employs dual advancements in computational algorithms and hardware-aware optimization. Notably, deep learning architectures have revolutionized the field of phase retrieval. Horisaki et al. [18] established neural wavefront regression using computational scattering models, achieving  $100\times$  speedup over iterative methods. Subsequent works like Lee et al. [25] enabled multi-depth holography through depth-conditioned networks, while Shi et al. [35] demonstrated real-time RGBD-to-hologram conversion using lightweight residual networks. These reported learning-driven methods, however, may struggle with generalizability across different optical setups.

Parallel to algorithmic innovations, the camera-in-the-loop (CITL) optimization [3, 33] addresses hardware imperfections through physical feedback. Recent studies have leveraged this feedback for applications including RGBD-based 3D holographic displays [11, 45], speckle noise reduction with partially coherent illumination [32], compact filter-free holographic displays [15, 45], off-axis optimization for HOEs [6, 7, 40], and integrated design with waveguides [16, 19]. We similarly incorporate camera-based feedback during result generation.

## 3 EYEBOX EXPANSION USING MULTI-ANGLE ILLUMINATION

The eyebox expansion scheme using multi-angle illumination is illustrated in the top-right of Fig. 1. The proposed design primarily comprises a laser array, a collimating lens (CL), a beam splitter (BS), an SLM, and an eyepiece. Unlike traditional collimated illumination, the laser array provides simultaneous multi-angle illumination to the SLM, creating multiple corresponding viewpoints magnified by the eyepiece for the human eye. As the pupil moves across these viewpoints, the holographic image remains continuously perceivable, effectively expanding the eyebox of the holographic near-eye display.

Specifically, as depicted in Fig. 1, the laser array located at the front focal plane of the CL emits multiple parallel beams that simultaneously illuminate the SLM. The SLM modulates these beams to construct a holographic image at an intermediate plane. This process of multi-angle modulation enables the generation of multiple viewpoints at the focal plane of the eyepiece. Upon magnification by the eyepiece, the holographic image is projected and focused onto the human retina.

With multi-angle illumination, various viewpoints are formed at the focal plane of the eyepiece, with the pitch  $p_e$  given by:

$$p_e = p_s \times \frac{f_e}{f_{cl}}, \quad (1)$$

where  $p_s$  is the laser array output interval,  $f_e$  and  $f_{cl}$  are the focal lengths of the eyepiece and collimating lens, respectively. The viewpoint pitch depends on the laser array interval and the focal length ratio of the eyepiece to the collimating lens. Multiple viewpoints are generated from the multi-angle illumination beams. When the pupil is within the viewpoint array region, the eyebox is efficiently expanded.

Notably, holographic images illuminated by different light sources are visible as the pupil moves or rotates. When the spacing between neighboring viewpoints exceeds the pupil size, only one viewpoint can enter the pupil at a time, forming a clear holographic image on the retina. This can cause a “black gap” effect as the pupil moves between neighboring viewpoints. Conversely, if the viewpoint spacing is smaller than the pupil size, light from multiple viewpoints may enter simultaneously, causing image aliasing. Multi-angle illumination on

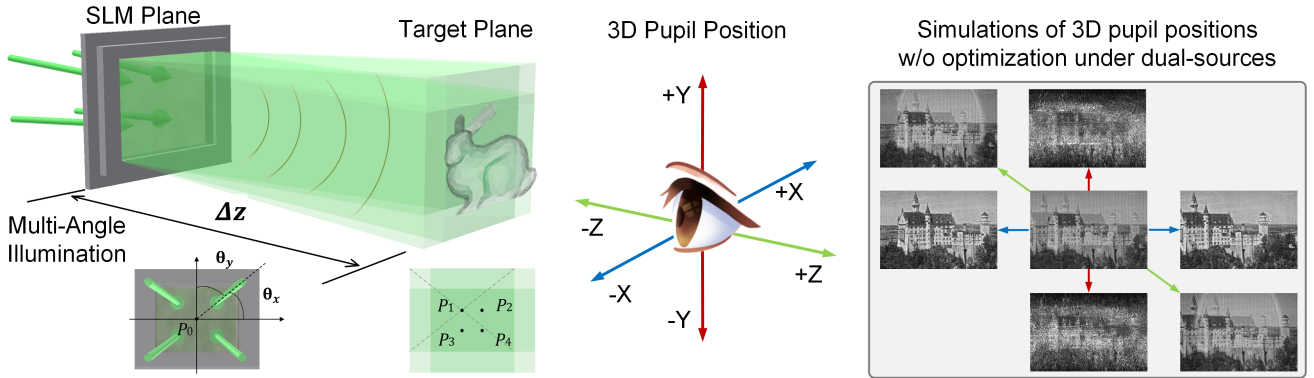


**Fig. 2:** **Left:** Schematic of propagation under multi-angle light illumination. The SLM is illuminated by the superposition of plane waves incident from four distinct angles. Four light sources hit the SLM plane on  $P_0$ , and to the target plane on  $P_1, P_2, P_3$ , and  $P_4$ . The parallel light waves, corresponding to their respective angles of inclination, superimpose at the same overlapping position on the target plane to reconstruct the image. **Right:** Without algorithmic optimization, under horizontal dual-sources, the pupil position is moved along X, Y, and Z axes for simulations. When positioned at the origin, image overlap occurs. With X-axis pupil displacement, the result is similar to single-light-source imaging. Displacement along the Y-axis significantly degrades image quality due to a lack of vertical light source expansion. Z-axis displacement creates image overlap with arc-shaped artifacts due to aperture effects.

the SLM generates overlapping holographic images on the retina, which reduces image quality. However, the coherent multi-angle illumination effectively multiplexes the SLM's pixels, optimizing its diffraction capabilities to avoid the “black gap” effect as the pupil moves.

We use a viewpoint spacing smaller than the pupil size to create a compact, continuous eyebox to ensure consistent, aligned holograms in near-eye displays. To address image aliasing introduced by the reduced spacing, a multi-angle illumination propagation framework is developed. This framework explicitly incorporates the dynamic pupil position and size to maintain consistent image quality across different viewpoints.

## 4 CUSTOMIZED HOLOGRAM GENERATION

### 4.1 Multi-angle-supported wave propagation

To obtain the correct hologram under multi-angle illumination, it is essential to model off-axis light propagation and the blending of multiple light sources, as illustrated in Fig. 2, using four-angle beams as an example. The SLM is illuminated by four light sources originating from  $P_0$ , towards the target plane at  $P_1, P_2, P_3$ , and  $P_4$ . The distance between the SLM plane and the target plane is denoted as  $\Delta z$ . Multiple beams share the same SLM pixels, simultaneously modulating off-axis illumination from various angles. The light modulation occurs on the same SLM region, but the beams are designed to be coherently superimposed on the target plane and thus imaged. The model focuses on off-axis propagation between parallel planes rather than traditional on-axis propagation.

In the calculation, the light field within the sampling window is first pre-shifted based on the tilt angle of each illumination beam [29, 30]. For the  $k^{th}$  beam out of  $N$  total beams, a phase factor  $\hat{\phi}_k$  corresponding to the tilted beam is added to achieve the desired offset. This phase factor simulates the effect of tilted parallel beam to generate shifted light field  $U_k(\varphi)$ :

$$U_k(\varphi) = U_{\text{SLM}}(\varphi) \exp \{i(\hat{\phi}_k)\}, \quad (2)$$

where  $U_{\text{SLM}}(\varphi)$  denotes the light field in the SLM plane and is analytically given by  $e^{i\varphi}$ . The shift-phase  $\hat{\phi}_k$  describes effect of the titled beam, shown as:

$$\hat{\phi}_k = \exp \left\{ i \frac{2\pi}{\lambda} (x \sin \theta_{x_k} + y \sin \theta_{y_k}) \right\}, \quad (3)$$

where  $\theta_{x_k}$  denotes the projection angle in the x-direction between the illumination and the propagation directions, while  $\theta_{y_k}$  represents the projection angle in the y-direction at the SLM plane.

The complex amplitude distribution  $u_k(x, y)$  in the target plane is computed using the angular spectrum method (ASM) [14]:

$$u_k(x, y) = \iint \mathcal{F}\{U_k(\varphi)\} \mathcal{H}(f_x, f_y; \Delta z) e^{i2\pi(f_x x + f_y y)} df_x df_y, \quad (4)$$

where  $\mathcal{F}\{\cdot\}$  represents the Fourier transform and  $\mathcal{H}(f_x, f_y; \Delta z)$  denotes the transfer function with propagation distance  $\Delta z$ .

Finally, the light field on the target plane for all illumination angles is superimposed to obtain the total light field under multi-angle illumination, expressed as:

$$u(x, y) = \sum_{k=1}^N u_k(x, y). \quad (5)$$

Using the above-described pipeline, we model light field propagation between the SLM and the target plane under multi-angle illumination. Once we obtain the angle of the  $N$  beams and propagation distance  $\Delta z$ , we can obtain the unique target light field  $u(x, y)$  after propagation of any light field  $U_{\text{SLM}}(\varphi)$  of the SLM plane.

### 4.2 Pupil-aware hologram optimization

Once the propagation relationship between the holographic and the target planes under multi-angle illumination is established, the hologram can be obtained by various optimization methods including the GS algorithm [44], the SGD algorithm [2], and their variants. Peng et al. [33] demonstrated that the naive SGD algorithm yields results comparable to or better than other iterative methods.

In addition to optimization schemes, hardware imperfection also affects display quality. Typical SLMs have a fill factor of around 0.9, which causes unwanted higher-order diffraction during reconstruction and requires additional optical filters to alleviate. However, to maintain the display's compact form factor, we apply an unfiltered holography optimization algorithm that simulates and thus addresses the higher-order diffraction during optimization, known as the higher-order gradient descent (HOGD) algorithm [15]. The human eye pupil functions as a dynamic low-pass filter, and by incorporating eye tracking, hologram generation algorithms that account for the pupil improve the display efficiency, an enhancement known as the Pupil-HOGD algorithm. Pupil-HOGD algorithm has been shown to significantly improve image quality in holographic near-eye displays [22].

Figure 3 illustrates the Pupil-HOGD algorithm under multi-angle illumination, where the wavefront's complex amplitude during propagation is shown in amplitude (black) and phase (blue). The values in the upper right of each complex amplitude represent the spatial or frequency domain dimensions, with  $N$  denoting the number of SLM pixels in that dimension and  $p$  the pixel pitch.  $\alpha$  indicates the number of higher-order diffractions.

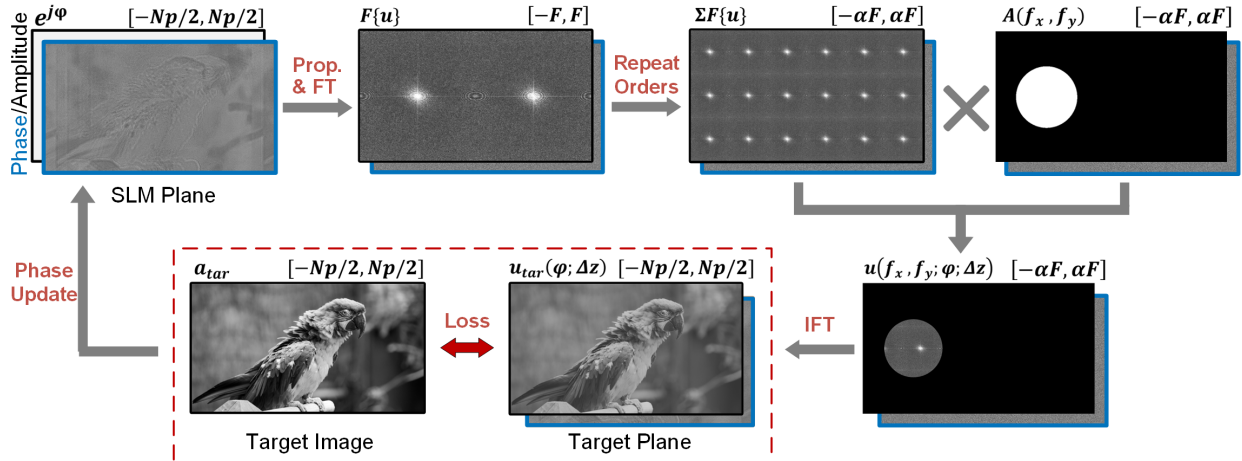


Fig. 3: Pipeline of Pupil-HOGD. Each wavefront is depicted with its amplitude (black) and phase (blue). Each dimension's spatial/frequency domain range is indicated, where  $N$  is the number of SLM pixels along the dimension, and  $p$  is the pixel pitch. The Fourier transform of the SLM wavefront is repeated in the frequency domain to consider high-order diffraction effects. This is then multiplied by a propagation kernel with attenuation and a pupil mask to generate the target wavefront. Finally, the loss function, comparing the target and the simulated images, is computed, and the phase pattern is updated through back-propagation using gradient descent.

Taking the dual light source as an example, the SLM plane light field  $e^{i\varphi}$  is first randomly initialized and then propagates to reconstruct the complex amplitude on the target plane  $u(x, y)$ , as described in Section 4.1. The spectral distribution  $F\{u(x, y)\}$  is then derived through the Fourier transform, resulting in two distinct centers on the spectral plane, each corresponding to one of the two angular light sources. In the absence of a filtering system, the propagation function is modified to simulate the higher-order diffraction of the SLM. The light field of the SLM plane is replicated in the frequency domain, which is denoted by  $u_{\text{unfilt}}(f_x, f_y; \varphi; \Delta z)$  [26]. Additionally, the finite square pixel pitch produces an attenuation of these frequency domain copies with a 2D *Sinc* function, the pupil produces a low-pass filtering effect  $M(f_x, f_y)$ , denoted by  $A(f_x, f_y)$ :

$$u_{\text{tar}}(\varphi; \Delta z) = \text{IFT}\{u_{\text{unfilt}}(f_x, f_y; \varphi; \Delta z)A(f_x, f_y)\},$$

$$u_{\text{unfilt}}(f_x, f_y; \varphi; \Delta z) = \sum_{i,j=-(\alpha-1)/2}^{(\alpha-1)/2} \mathcal{F}\{u(x, y)\} \left( f_x + \frac{i}{p}, f_y + \frac{j}{p} \right),$$

and  $A(f_x, f_y) = \text{sinc}(\pi f_x p) \text{sinc}(\pi f_y p) M(f_x, f_y)$ . (6)

In Eq. 6, the pupil mask  $M(f_x, f_y)$  enables the phase to be optimized while considering the filtering effect performed by the pupil. When the pupil diameter is  $D_p$  and the focal length of the eyepiece is  $F$ ,  $M(f_x, f_y)$  acts as a filter in the Fourier domain with a circular filter of a diameter  $D_p/\lambda F$ , for which the inner frequency of the circular filter is 1 and otherwise 0. The product of  $u_{\text{unfilt}}(f_x, f_y; \varphi; \Delta z)$  and  $A(f_x, f_y)$  is transmitted back to the spatial domain by the inverse Fourier transform (IFT) to obtain the light field  $u_{\text{tar}}(\varphi; \Delta z)$  in the target plane. With this Pupil-HOGD propagation model, all of the orders can be optimized. This is performed by minimizing the squared  $\mathcal{L}_2$  loss in Eq. 7 with gradient descent, where  $s$  is a global scale factor and  $a_{\text{tar}}$  is the target amplitude  $|u_{\text{tar}}|$ , yields:

$$\text{argmin}_{\varphi, s} \|s \cdot |u_{\text{tar}}(\varphi; \Delta z)| - a_{\text{tar}}\|_2^2. \quad (7)$$

Pupil-HOGD modifies the forward propagation process to account for phase shifts in multi-angle illumination, hardware-induced filtering, and higher-order diffraction. To evaluate its effectiveness in incorporating pupil and higher-order diffraction, the SGD, HOGD, and Pupil-HOGD algorithms were simulated for hologram optimization. Simulations used dual-angle illumination with angles of  $(+0.7125^\circ, 0^\circ)$  and  $(-0.7125^\circ, 0^\circ)$ . The pupil diameter  $D_p$  was set to 3.125 mm, with positions at  $(-1.5 \text{ mm}, 0 \text{ mm})$ ,  $(0 \text{ mm}, 0 \text{ mm})$ , and  $(1.5 \text{ mm}, 0 \text{ mm})$ , respectively. The distance  $\Delta z$  between the SLM and the target planes was fixed at 80 mm.

In the study, we used two datasets, DIV2K [1] and Corel5k [13], each providing 100 selected images that have been normalized to a resolution of  $1920 \times 1080$  pixels. The holograms were optimized using the SGD, HOGD, and Pupil-HOGD algorithms, and simulated reconstructions were evaluated using peak signal-to-noise ratio (PSNR). Results were averaged for each algorithm and dataset, as summarized in Table 1. Pupil-HOGD consistently achieved the highest PSNR across both datasets.

Table 1: Result comparison of optimization algorithms across two datasets. We selected and normalized 100 images from DIV2K and Corel5k, which were processed using SGD, HOGD, and Pupil-HOGD algorithms. Average PSNR(dB)/SSIM are presented.

Algorithms	SGD	HOGD	Pupil-HOGD
DIV2K	13.82 / 0.27	17.52 / 0.34	32.15 / 0.84
Corel5k	13.74 / 0.25	17.16 / 0.33	30.98 / 0.78

Figure 4 presents the results for a specific image, showcasing different pupil positions and optimization algorithms. The pupil positions in each row are  $(-1.5 \text{ mm}, 0 \text{ mm})$ ,  $(0 \text{ mm}, 0 \text{ mm})$ , and  $(1.5 \text{ mm}, 0 \text{ mm})$ . The first column illustrates the pupil position in the frequency domain, while the second to fourth columns display results for different algorithms. The fifth column shows holograms optimized using the Pupil-HOGD algorithm. SGD algorithm produces the lowest PSNR for all pupil positions as it disregards higher-order diffraction. The HOGD algorithm performs slightly better by accounting for higher-order diffraction but neglects the pupil's low-pass filtering effect. In contrast, the Pupil-HOGD algorithm achieves the highest PSNR by incorporating the pupil's constraints on light source utilization across different angles. Notably, the PSNR reaches 38 dB for pupil positions at both  $(-1.5 \text{ mm}, 0 \text{ mm})$  and  $(+1.5 \text{ mm}, 0 \text{ mm})$ .

The relationship between image quality and pupil position across the three algorithms is not linear. To further investigate their characteristics, we have varied both the pupil position and size. Figure 5 presents a simulated comparison for different algorithms at various pupil positions. Different colors represent different methods: purple for Pupil-HOGD, blue for HOGD, and yellow for SGD. Line styles denote pupil size: solid for  $D_p=3 \text{ mm}$ , dashed for  $D_p=2 \text{ mm}$ , and dotted for  $D_p=4 \text{ mm}$ . The horizontal axis corresponds to the pupil position along the X-direction, while the vertical axis indicates the PSNR (See Supplement Sec. 4).

The results demonstrate that a larger pupil generally improves image quality, though exceptions exist. For example, when the Pupil-HOGD algorithm is applied at a pupil position  $(\pm 1.0 \text{ mm}, 0 \text{ mm})$ , the correlation between pupil size and image quality reverses. The Pupil-HOGD

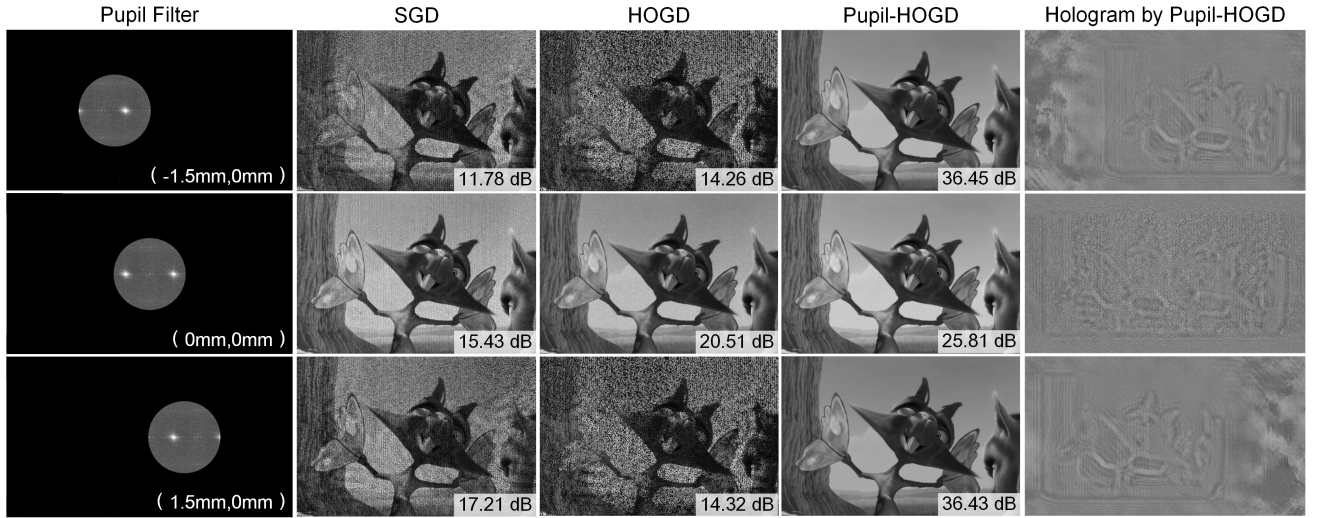


Fig. 4: Comparison of hologram optimization algorithms across various pupil positions. Each row corresponds to pupil positions at (-1.5 mm, 0 mm), (0 mm, 0 mm), and (1.5 mm, 0 mm). The first column visualizes the pupil position in the frequency domain, while columns two to four display the results of the SGD, HOGD, and Pupil-HOGD algorithms, respectively. The fifth column showcases the optimized hologram using the Pupil-HOGD algorithm. The SGD algorithm yields the lowest PSNR due to neglecting higher-order diffraction. In contrast, the HOGD algorithm slightly improves but still ignores the pupil's low-pass filtering effect. The Pupil-HOGD algorithm outperforms the others by accounting for the constraining effect of pupil position on light source utilization at various angles.

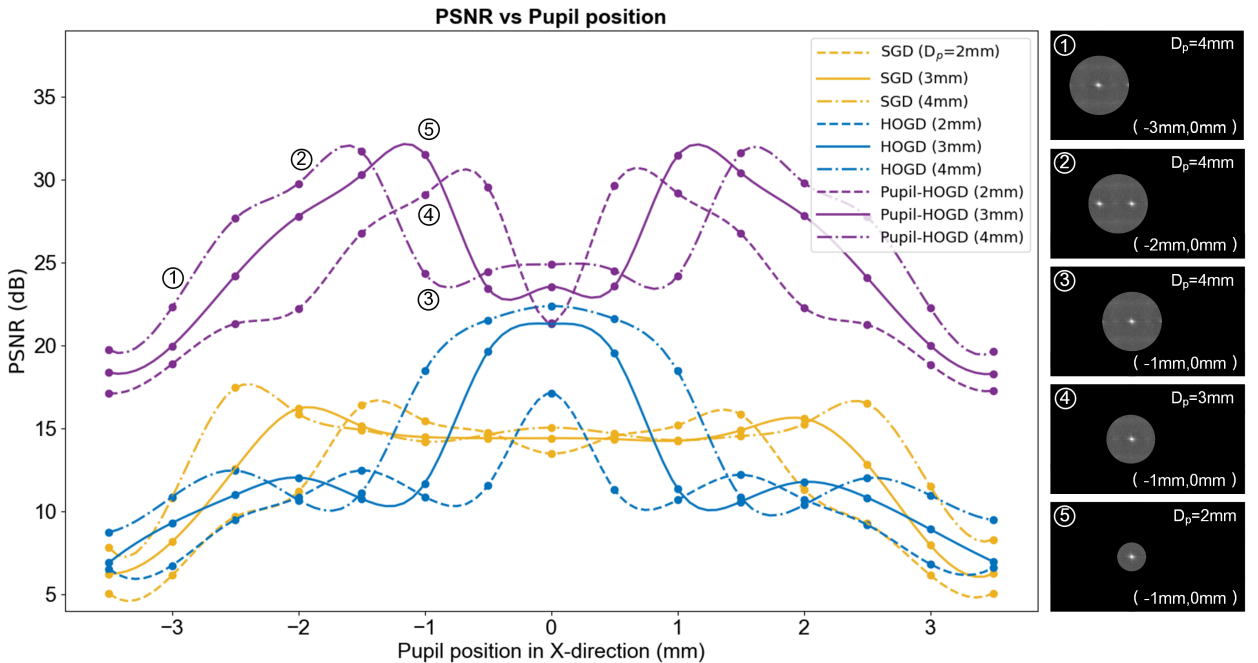


Fig. 5: Comparison of simulated images generated by various algorithms with varying pupil positions under dual-angle illumination, evaluated using the PSNR metric. Here, the purple plot represents Pupil-HOGD, blue represents HOGD, and yellow represents SGD. The x-axis indicates the pupil position along the x-direction of the reconstruction, with different line styles denoting the pupil size. The Pupil-HOGD algorithm achieves the best results at all positions, particularly at ( $\pm 1.5$  mm, 0 mm), where dual-light source interference is minimal. In contrast, the Pupil-HOGD algorithm performs slightly worse at (0 mm, 0 mm) due to light interference from dual sources. HOGD better predicts the image quality on actual display than SGD as it accounts for higher diffraction orders. Additionally, a larger pupil preserves more information in frequency-domain, enhancing image reconstruction quality.

algorithm, which incorporates pupil aperture modeling, consistently delivers the best image quality across all pupil positions. However, at the center position (0.0 mm, 0.0 mm), Pupil-HOGD performs suboptimally, due to multi-angle illumination, which causes a shift in the light wave within the frequency domain, and results in information loss. We highlight five key points on the curve and show the corresponding pupil filtering effects in the frequency domain on the right.

## 5 IMPLEMENTATION

### 5.1 Experimental setup

Prior to constructing the experimental setup, we conducted simulations to evaluate image quality under varying parameters, including different tilt angles and numbers of light sources. While image quality might decrease as either the tilt angle or the number of light sources increases, high image quality is preserved with two distinct light source angles, which significantly enlarges the eyebox (see Supplement Sec. 3 for more details).

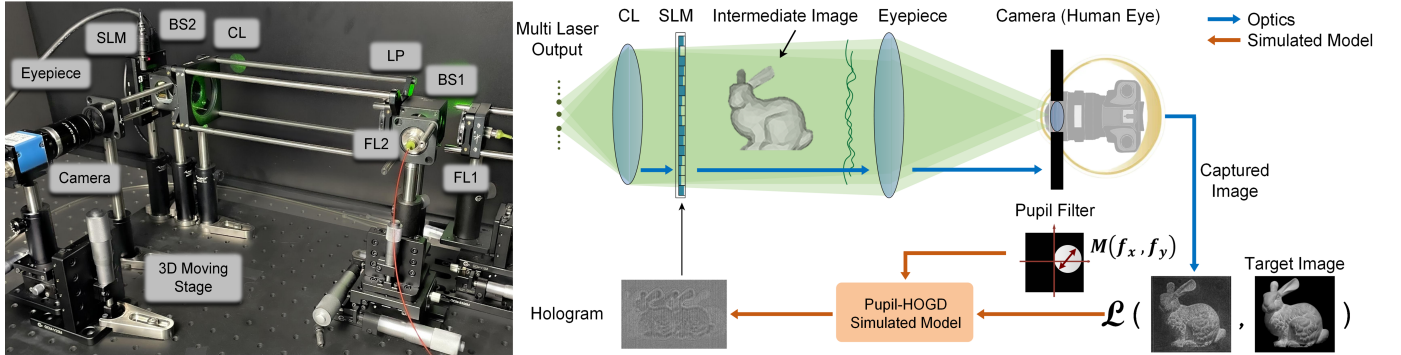


**Fig. 6:** **Left:** Display prototype. Two fiber laser (FL) outputs pass through a beam splitter (BS), linear polarizer (LP), and collimating lens (CL) to illuminate the SLM. The target image is magnified by the eyepiece and captured by an industrial camera, simulating the human eye. The camera is mounted on a 3D moving stage to measure the eyebox. **Right:** Schematic of the Pupil-HOGD with CITL calibration process. The light field in the target plane is formed by the superposition of multi-angle illumination. A camera with a lens simulates the human eye, with its aperture representing the pupil size, and captures the reconstructed image as the feedback. The loss between the amplitude of the captured image and the target image is computed, and the phase is iteratively updated through back-propagation until convergence. Pupil size is incorporated in the back-propagation as a filter  $M(f_x, f_y)$  in the frequency domain.

We built an experimental prototype using laser light sources from two distinct angles, as shown in Fig. 3. The bench-top prototype consists of a UPOlabs SLM (HDSLM64R,  $1,920 \times 1,080$ ,  $p = 6.4 \mu\text{m}$ ), a Lubon linear polarizer (FLP25-VIS-M), a Thorlabs beam splitter (BS013), a DaHeng beam splitter (GCC-401102), a Thorlabs fiber coupler (PN530R5A1), a 3D moving stage, a laser source (MGL-III-532-50 mW), a Unified Optics collimating lens (VISN-BK7/SF2,  $f_L = 300$  mm), an eyepiece (DaHeng GCL-010652), and an Imaging Source camera (DFK33UX174) with a lens ( $f_L = 50$  mm,  $D = 3.125$  mm).

To evaluate the impact of propagation distance on image quality, the propagation distance was set to 110 mm. The illumination light's tilt angle was selected as  $1.2^\circ$  to achieve the desired eyebox expansion. When the focal length of the eyepiece is 50 mm, the FOV is  $16.05^\circ$ . All components are mounted using cage bar connections to ensure precise optical alignment. The software part was run on an Nvidia RTX 3090 graphics card, with the content corresponding to each illumination alternately optimized to limit memory usage. The computational time for single-phase pattern generation with 500 iterations using Pupil-HOGD on a PC was 4 minutes. Device specifications and models are provided in Table 2.

The system workflow is as follows: A laser beam is split into two coherent beams using a fiber coupler, with each directed to the focal plane of a collimating lens, delivering parallel illumination at distinct angles to expose the SLM simultaneously. The SLM modulates the light, and the resulting images are captured by a camera positioned after an eyepiece. The fiber outputs are mounted on a 3D translation stage, allowing precise adjustment of the illumination angles during experimentation. Polarizers are placed at the output of each fiber to control the relative brightness between the two light sources and to align their polarization state with that of the SLM. Employing a camera in place of the human eye facilitates the implementation of the CITL calibration strategy.

Table 2: Specifications of prototype parts.

Components	Model & Spec.
Laser	MGL-III-532-50mW
Fiber Coupler	THORLABS PN530R5A1
BS 1	THORLABS BS013
BS 2	DaHeng GCC-401102
Polarizer	LUBON FLP25-VIS-M
Collimating lens	UNIFIED OPTICS VISN-BK7/SF2
SLM	UPOlabs HDSLM64R
Eyepiece	DaHeng GCL-010652
Camera	Imaging Source DFK33UX174

## 5.2 Pupil-HOGD with camera calibration

During hologram optimization, wavefront propagation with the idealized assumptions may not fully reflect the experimental system. This discrepancy constitutes the primary factor underlying the observed image degradation. To this end, we employ the CITL approach, an established calibration strategy that has demonstrated effectiveness in computer-generated holography [33]. Specifically, we introduce an optimization framework under multi-angle illumination that integrates the Pupil-HOGD algorithm with CITL calibration, effectively bridging the gap between ideal model and real-world hardware, thereby enabling high-fidelity holographic reconstruction across a range of pupil sizes and positions.

The forward/backward propagation in the Pupil-HOGD simulation is as illustrated in Fig. 3. In the CITL calibration scheme, the forward propagation is supplanted by actual optical propagation. The complete optimization process is depicted on the right of Fig. 6, where blue arrows represent physical optical forward propagation and orange arrows denote the image processing for back-propagation simulation. During optical forward propagation, the SLM modulates multiple inclined laser beams after collimation, forming an intermediate image. This image is relayed by an eyepiece and captured by a camera equipped with a lens positioned at the Fourier plane of the intermediate image. The lens aperture filters the spatial frequency information of light wave, functioning as both a pupil filter described by  $M(f_x, f_y)$  in Pupil-HOGD and an analog for the human eye's pupil. This configuration ensures the alignment between hardware system and algorithm. Additionally, the camera sensor operates as a proxy for the human retina, allowing the captured image to undergo model-based back-propagation.

The corrected loss, which incorporates the pupil filter, is back-propagated to the SLM plane. Auto-differentiation is employed to optimize the phase hologram. Starting with an initial estimate  $\phi_i$ , the model performs forward propagation, evaluates the loss function  $\mathcal{L}$ , and back-propagates the error using the gradient  $\frac{\partial \mathcal{L}}{\partial \phi}$  to update  $\phi_{i+1}$ . Notably, this CITL-empowered optimization incorporates optical wave propagation  $\hat{f}$ , as follows:

$$\phi_{i+1} \leftarrow \phi_i - \alpha \left( \frac{\partial \mathcal{L}_i}{\partial \phi} \right)^T, \quad \mathcal{L}_{i+1} \approx \phi_i - \alpha \left( \frac{\partial \mathcal{L}_i}{\partial f} \cdot \frac{\partial \hat{f}}{\partial \phi} \right)^T \mathcal{L}_i, \quad (8)$$

where  $\alpha$  is the learning rate. The gradients are approximated using the model proxy  $\frac{\partial \hat{f}}{\partial \phi}$ . The term  $\frac{\partial \mathcal{L}_i}{\partial f}$  is efficiently computed by inputting the captured image into a loss function with automatic differentiation enabled. Through iterative cycles of optical forward-propagation and model-based back-propagation, the phase is continuously updated until the loss converges.

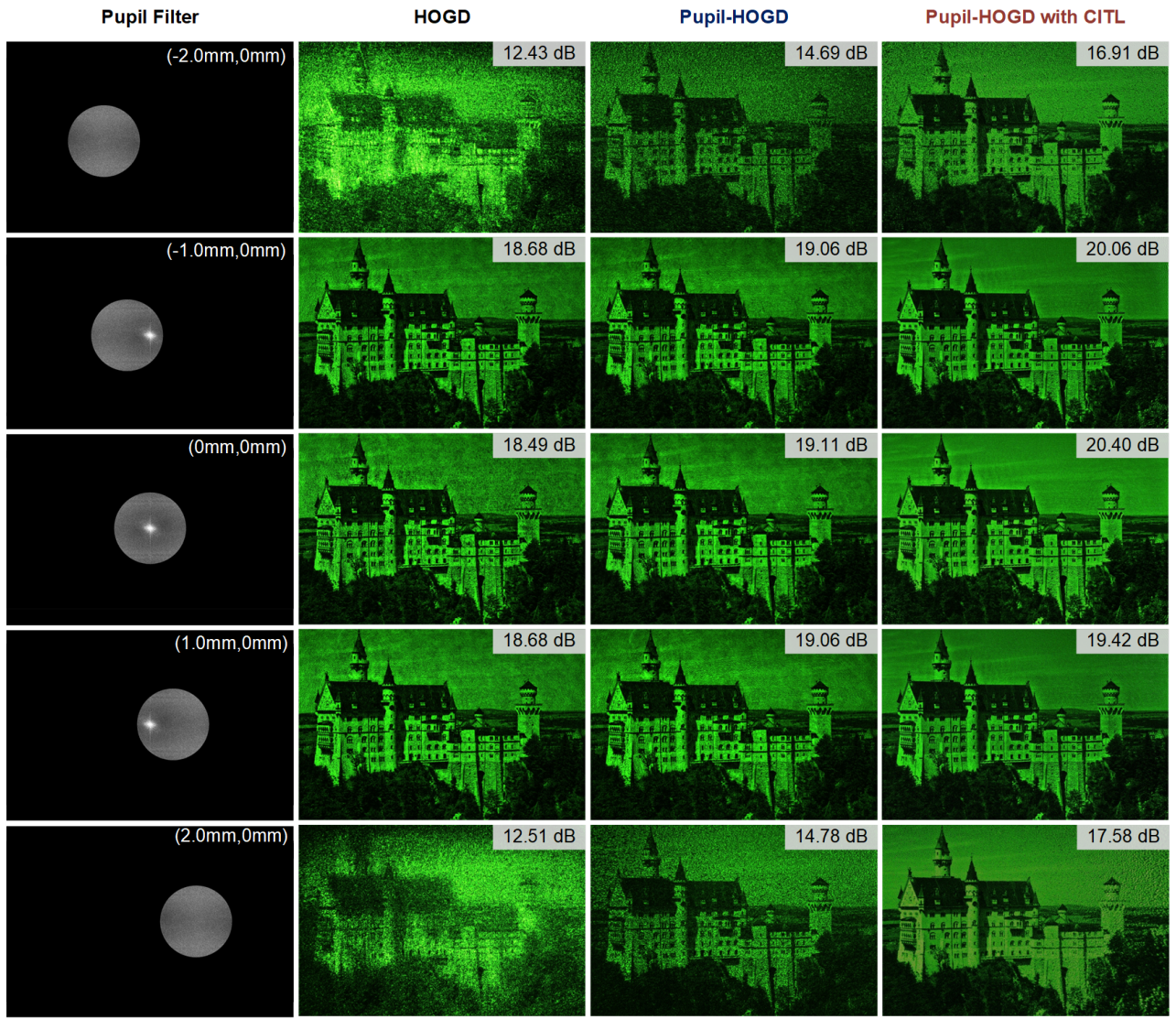


Fig. 7: Experimental results of HOGD, Pupil-HOGD, and Pupil-HOGD with CITL algorithm at various pupil positions under single-angle illumination. The pupil positions range from -2 mm to 2 mm in 1 mm intervals. The first column shows the frequency-domain filtering corresponding to different pupil positions. The second column displays the HOGD result, where pupil constraints are not incorporated into the algorithm. The third column presents the Pupil-HOGD results, which include the pupil's constraints in the optimization process. The fourth column illustrates the Pupil-HOGD-CITL result, where camera calibration further enhances Pupil-HOGD performance.

## 6 EXPERIMENTAL RESULTS

### 6.1 Validation with single-angle illumination

To evaluate the horizontal eyebox under coaxial single-light-source illumination, we have assessed the HOGD, Pupil-HOGD, and Pupil-HOGD with CITL algorithms at various pupil positions using the previously described experimental setup as shown in Fig. 7. In Column 1, the horizontal pupil filter is shifted from -2.0 mm to 2.0 mm in 1.0 mm increments. Column 2 highlights HOGD's limitations: as the pupil shifts, the image background becomes increasingly noisy due to high-frequency information loss. At (-1.0 mm, 0 mm) and (1.0 mm, 0 mm), pupil edges approach low-frequency bright spots, causing pronounced quality degradation. At extreme positions ( $\pm 2.0$  mm, 0 mm), image contours are severely obscured, although images remain observable with compromised detail. Column 3 demonstrates the improvements offered by Pupil-HOGD's through spectral energy redistribution. Even at extreme positions ( $\pm 2.0$  mm, 0 mm), it enables better information transfer than standard HOGD. However, peripheral images still suffer from scattering noise and detail loss. Column 4 presents results from Pupil-HOGD with CITL calibration, addressing simulation-hardware discrepancies. CITL implementation markedly reduces artifacts and

background noise, particularly improving sky regions' uniformity and contrast. While positions ( $\pm 1.0$  mm, 0 mm) retain some contrast loss, CITL unexpectedly recovers high-frequency information at ( $\pm 2.0$  mm, 0 mm), even when the viewpoint extends beyond the nominal pupil boundary (refer to Supplement Sec. 4). The Pupil-HOGD with CITL approach achieves clear image reproduction across the full -2.0 mm to 2.0 mm range, validating Pupil-HOGD's effectiveness under single-light-source conditions.

### 6.2 Eyebox expansion with multi-angle illumination

Additional experiments under multi-angle illumination evaluated eyebox expansion. Illumination angles ( $\pm 1.2^\circ$ ,  $0^\circ$ ) created  $12.8 \mu\text{m}$  fringe periods (See Supplement Sec. 1), with a 110 mm propagation distance enabling 2 mm viewpoint separation (1 mm extension per side). Using a 3.125 mm pupil moved from -3.5 mm to 3.5 mm in 0.5 mm increments (15 images total; Supplement Sec. 5), Fig. 8 shows enhanced multi-angle results.

Column 1 displays pupil movement from -3.0 mm to 3.0 mm (1.5 mm steps), revealing two occasional zero-order diffraction patterns – a key multi-angle distinction. Column 2 shows Pupil-HOGD reconstructions with expanded eyebox boundaries, but quality declines

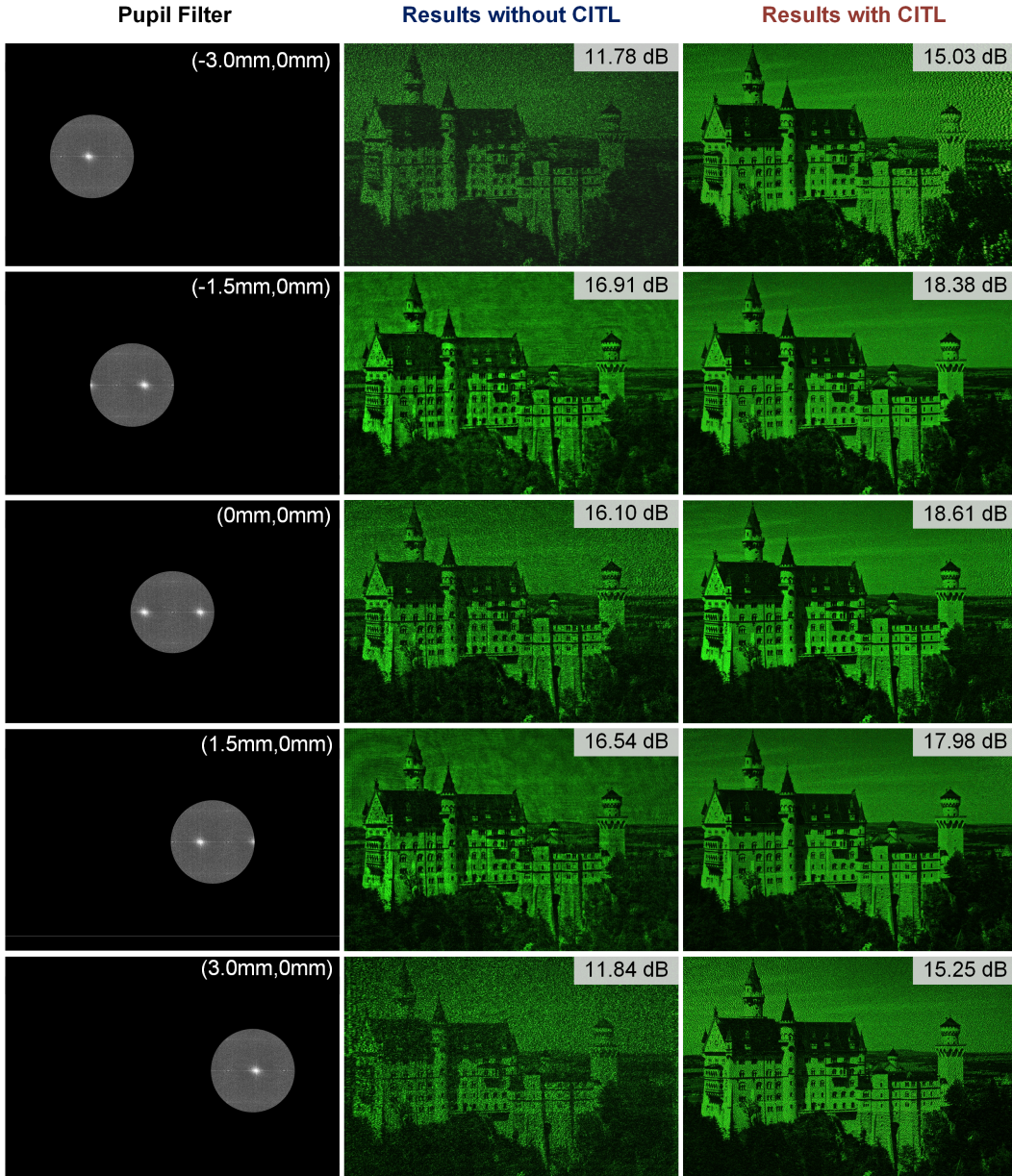


Fig. 8: Experimental results of Pupil-HOGD, and Pupil-HOGD with the CITL algorithm at various pupil positions under dual-angle illumination. Pupil positions range from -3.0 mm to 3.0 mm in 1.5 mm intervals. The first column illustrates the frequency-domain filtering results for different pupil positions. The second column presents the results of Pupil-HOGD. The third column shows the results of Pupil-HOGD with CITL calibration. Compared to single-angle illumination, dual-angle illumination extends the eyebox by 50%.

at  $(\pm 3.0 \text{ mm}, 0 \text{ mm})$  as viewpoints exit the pupil. Column 3 demonstrates Pupil-HOGD with CITL improvements, achieving peak PSNR at  $(\pm 1.5 \text{ mm}, 0 \text{ mm})$  rather than the center (Fig. 5). The combined approach enables complete castle visibility across  $\pm 3.0 \text{ mm}$  horizontally 50% larger eyebox than single-angle illumination, while maintaining high image quality.

## 7 DISCUSSION AND CONCLUSION

This work has presented a novel approach to enhancing holographic near-eye displays' capability by addressing two primary challenges: expanding the eyebox and augmenting image quality. This is achieved by implementing multi-angle illumination and establishing the Pupil-HOGD phase-only hologram generation algorithm. As a result, at the stage of proof-of-concept, we have successfully extended the eyebox by 50% in the horizontal direction with dual-angle illumination. Additionally, the integration of pupil-aware hologram optimization has notably improved image fidelity, particularly in scenarios where multiple fo-

cal points penetrate the pupil. Moving a step further, incorporating the CITL calibration into the Pupil-HOGD algorithm ensures minimal disparities between theoretical simulations and actual hardware performance, leading to visually accurate and high-quality holographic reconstruction. Experimental results tested on a bench-top holographic display prototype with dual-illumination configuration demonstrate substantial enhancements in both image quality and eyebox. These advancements offer a promising pathway toward the development of high-quality, immersive visual experiences.

### 7.1 Bells & Whistles

Our pupil-adaptive framework redefines étendue expansion by balancing performance with hardware simplicity. Unlike Chao et al.'s dual-SLM Fourier modulation—which achieves  $2 \times$  étendue expansion but requires intricate hardware alignment and lacks pupil compensation [4]—our single-SLM, multi-angle illumination preserves phase fidelity and adapts dynamically to pupil movement. Kuo et al.'s dual-

SLM design achieves strong speckle suppression [24] but emphasizes static image quality over étendue scalability and disregards pupil mobility. Tseng et al.'s neural étendue expanders achieve impressive  $64 \times$  gains [36], yet are limited by fixed post-fabrication optical responses and chromatic drift. In contrast, our Pupil-HOGD algorithm continuously refines output through CITL calibration, enabling robust adaptation.

For energy consumption, our dual-source illumination achieves comparable average power efficiency (13.27%) within the entire supported eyebox to the traditional single-source approach (14.53%). Detailed energy efficiency with different pupil locations are provided in Supplementary Sec. 2.

Critically, our method achieves a 50% eyebox expansion with a single SLM, an essential trade-off for AR/VR applications where motion tolerance and compact form factors are key. Future systems could integrate Chao's spatial multiplexing, Kuo's speckle suppression, and Tseng's étendue scaling with our pupil-aware optimization to enable greater eyebox expansion with real-time adaptability.

## 7.2 Follow-up Work

We note that the following aspects warrant further investigation.

**Fast hologram generation with robust eye-tracking.** The proposed holographic displays under multi-angle illumination require real-time hologram updates based on pupil position and size. This necessitates integrating robust eye-tracking with a real-time CGH algorithm for practical deployment. However, the current Pupil-HOGD algorithm relies on iterative optimization using the CITL strategy, which remains computationally intensive. Future work could explore lightweight neural networks as a replacement for CITL-based Pupil-HOGD.

Three recent advances offer promising directions. First, Dong et al.'s *divide-conquer-and-merge* strategy partitions a  $1,920 \times 1,080$  SLM into parallel subregions, reducing GPU memory usage by 64.3% and speeding up computation  $3 \times$  without sacrificing image fidelity [12]. This aligns well with our spatially constrained pupil model. Second, Zhou et al.'s 3D-HoloNet achieves 30 fps full-HD holograms via camera-calibrated learning [45]. Their use of phase regularization and unfiltered propagation model closely mirrors our Pupil-HOGD framework; fine-tuning 3D-HoloNet with our CITL dataset could reduce latency while maintaining quality. Third, Yeom et al.'s PoFNet demonstrates CITL-optimized amplitude modulation in Fourier space, effectively reducing noise without requiring physical filters [42].

**Full-color 3D display potential.** On the one hand, our validation experiments were conducted using a laser with a wavelength of 532 nm, which limits the prototype to a monochrome display. To facilitate full-color holographic displays, our plans include incorporating RGB lasers and synchronizing them with the high-frame-rate SLM. On the other hand, although the prototype supports 3D depth cues, the validations in this study were primarily focused on a single desired target distance. Future work can involve using RGBD images to assess the prototype's 3D reconstruction capabilities, as demonstrated in state-of-the-art work [10, 11].

**Compact form factor with a wide FOV.** In our experiments, the FOV of the bench-top prototype is  $16.1^\circ$  diagonally, primarily determined by the eyepiece's numerical aperture (NA) and the utilized SLM's size. The FOV of the prototype is relatively small for practical applications. Optical devices with higher NA, such as off-axis HOE combiners, metasurfaces, or metasurface combiners, offer significant benefits for expanding the FOV. In addition, the current form factor of the prototype is bulky for practical use. By integrating optical devices such as off-axis HOEs [39], we can substantially reduce the form factor, allowing eyeglass-style holographic near-eye displays with wider FOV. In future work, we aim to incorporate off-axis HOE combiners to achieve both a compact form factor and an expanded FOV (See Supplement Sec. 6).

**Vertical eyebox expansion.** We acknowledge that vertical pupil movement is a critical factor influencing user experience for near-eye displays. Our proposed multi-angle illumination framework inherently supports both horizontal and vertical eyebox expansion via orthogonal orthogonally arranged light source. Simulations confirm this capability

(see Supplementary Figs. 8–10), though practical realization is currently limited by image quality degradation arising from zero-order interference aliasing under multi-source configurations. Importantly, the Pupil-HOGD algorithm already leverages the full 3D pupil coordinates, facilitating seamless vertical adaptation as eye-tracking technologies continue to advance.

## ACKNOWLEDGMENTS

This research was supported by the Science and Technology Commission of Shanghai Municipality (24511106502), National Science Foundation of China (62322217, 62005154), the National Key Research and Development Program of China (2021YFB2802200), Research Grants Council of Hong Kong (GRF 17208023), and the Natural Science Foundation of Shanghai (20ZR1420500).

## REFERENCES

- [1] E. Agustsson and R. Timofte. Ntire 2017 challenge on single image super-resolution: Dataset and study. In *2017 IEEE Conference on Computer Vision and Pattern Recognition Workshops (CVPRW)*, pp. 1122–1131, 2017. doi: 10.1109/CVPRW.2017.150 [4](#)
- [2] P. Chakravarthula, Y. Peng, J. Kollin, H. Fuchs, and F. Heide. Wirtinger holography for near-eye displays. *ACM Trans. Graph.*, 38(6):213:1–213:13, Nov. 2019. doi: 10.1145/3355089.3356539 [3](#)
- [3] P. Chakravarthula, E. Tseng, T. Srivastava, H. Fuchs, and F. Heide. Learned hardware-in-the-loop phase retrieval for holographic near-eye displays. *ACM Transactions on Graphics (TOG)*, 39(6):1–18, 2020. [2](#)
- [4] B. Chao, M. Gopakumar, S. Choi, J. Kim, L. Shi, and G. Wetzstein. Large étendue 3d holographic display with content-adaptive dynamic fourier modulation. In *SIGGRAPH Asia 2024 Conference Papers*, pp. 1–12, 2024. [2, 8](#)
- [5] B. Chao, M. Gopakumar, S. Choi, J. Kim, L. Shi, and G. Wetzstein. Large Étendue 3d holographic display with content-adaptive dynamic fourier modulation. In *SIGGRAPH Asia 2024 Conference Papers*, SA '24. ACM, New York, NY, USA, 2024. doi: 10.1145/3680528.3687600 [2](#)
- [6] C. Chen, D. Kim, D. Yoo, B. Lee, and B. Lee. Off-axis camera-in-the-loop optimization with noise reduction strategy for high-quality hologram generation. *Opt. Lett., OL*, 47(4):790–793, Feb. 2022. doi: 10.1364/OL.447871 [2](#)
- [7] L. Chen, R. Zhu, and H. Zhang. Speckle-free compact holographic near-eye display using camera-in-the-loop optimization with phase constraint. *Opt. Express*, 30(26):46649–46665, Dec. 2022. doi: 10.1364/OE.475066 [2](#)
- [8] T. Chen, Z. Wang, Y. Wang, Q. Feng, and G. Lv. Multiple viewpoints optimization for holographic near-eye display based on a pupil mask. *Optics & Laser Technology*, 179:111400, 2024. doi: 10.1016/j.optlastec.2024.111400 [1](#)
- [9] M.-H. Choi, Y.-G. Ju, and J.-H. Park. Holographic near-eye display with continuously eyebox using two-dimensional replication and angular spectrum wrapping. *Optics Express*, 28(1):533–547, 2020. doi: 10.1364/OE.381277 [1, 2](#)
- [10] S. Choi, M. Gopakumar, Y. Peng, J. Kim, M. O'Toole, and G. Wetzstein. Time-multiplexed neural holography: A flexible framework for holographic near-eye displays with fast heavily-quantized spatial light modulators. In *ACM SIGGRAPH 2022 Conference Proceedings*, SIGGRAPH '22. ACM, New York, NY, USA, 2022. doi: 10.1145/3528233.3530734 [9](#)
- [11] S. Choi, M. Gopakumar, Y. Peng, J. Kim, and G. Wetzstein. Neural 3D holography: learning accurate wave propagation models for 3D holographic virtual and augmented reality displays. *ACM Trans. Graph.*, 40(6):240:1–240:12, Dec. 2021. doi: 10.1145/3478513.3480542 [2, 9](#)
- [12] Z. Dong, J. Jia, Y. Li, and Y. Ling. Divide-conquer-and-merge: Memory- and time-efficient holographic displays. In *2024 IEEE Conference Virtual Reality and 3D User Interfaces (VR)*, pp. 493–501. Orlando, FL, USA, 2024. doi: 10.1109/VR58804.2024.00070 [9](#)
- [13] P. Duygulu, K. Barnard, J. de Freitas, and D. Forsyth. Corel5k dataset. <https://rdrr.io/cran/mldr.datasets/man/core15k.html>, 2002. [4](#)
- [14] J. W. Goodman. *Introduction to Fourier optics*. 2005. doi: 10.1063/1.3035549 [3](#)
- [15] M. Gopakumar, J. Kim, S. Choi, Y. Peng, and G. Wetzstein. Unfiltered holography: optimizing high diffraction orders without optical filtering for compact holographic displays. *Opt. Lett., OL*, 46(23):5822–5825, Dec. 2021. doi: 10.1364/OL.442851 [2, 3](#)

- [16] M. Gopakumar, G.-Y. Lee, S. Choi, B. Chao, Y. Peng, J. Kim, and G. Wetzstein. Full-colour 3d holographic augmented-reality displays with meta-surface waveguides. *Nature*, 629(8013):791–797, 2024. [2](#)
- [17] D. M. Hoffman, A. R. Girshick, K. Akeley, and M. S. Banks. Vergence-accommodation conflicts hinder visual performance and cause visual fatigue. *Journal of Vision*, 8(3):33, Mar. 2008. doi: 10.1167/8.3.33 [1](#)
- [18] R. Horisaki, R. Takagi, and J. Tanida. Deep-learning-generated holography. *Appl. Opt.*, 57(14):3859–3863, May 2018. doi: 10.1364/AO.57.003859 [2](#)
- [19] C. Jang, K. Bang, M. Chae, B. Lee, and D. Lanman. Waveguide holography for 3d augmented reality glasses. *Nature Communications*, 15(1):66, 2024. [2](#)
- [20] C. Jang, K. Bang, G. Li, and B. Lee. Holographic near-eye display with expanded eye-box. *ACM Trans. Graph.*, 37(6), Dec. 2018. doi: 10.1145/3272127.3275069 [1, 2](#)
- [21] Y. Jo, C. Yoo, K. Bang, B. Lee, and B. Lee. Eye-box extended retinal projection type near-eye display with multiple independent viewpoints [Invited]. *Applied Optics*, 60(4):A268–A276, Feb. 2021. doi: 10.1364/AO.408707 [2](#)
- [22] J. Kim, M. Gopakumar, S. Choi, Y. Peng, W. Lopes, and G. Wetzstein. Holographic glasses for virtual reality. In *ACM SIGGRAPH 2022 Conference Proceedings*, SIGGRAPH '22. ACM, New York, NY, USA, 2022. doi: 10.1145/3528233.3530739 [1, 3](#)
- [23] T. Kozacki, M. Kujawińska, G. Finke, B. Hennelly, and N. Pandey. Extended viewing angle holographic display system with tilted SLMs in a circular configuration. *Appl. Opt., AO*, 51(11):1771–1780, Apr. 2012. doi: 10.1364/AO.51.001771 [1, 2](#)
- [24] G. Kuo, L. Waller, R. Ng, and A. Maimone. High resolution étendue expansion for holographic displays. *ACM Trans. Graph.*, 39(4):66:66:1–66:66:14, Aug. 2020. doi: 10.1145/3386569.3392414 [2, 9](#)
- [25] J. Lee, J. Jeong, J. Cho, D. Yoo, B. Lee, and B. Lee. Deep neural network for multi-depth hologram generation and its training strategy. *Opt. Express*, 28(18):27137–27154, Aug 2020. doi: 10.1364/OE.402317 [2](#)
- [26] G. Li, J. Jeong, D. Lee, J. Yeom, C. Jang, S. Lee, and B. Lee. Space bandwidth product enhancement of holographic display using high-order diffraction guided by holographic optical element. *Opt. Express*, 23(26):33170–33183, Dec 2015. doi: 10.1364/OE.23.033170 [4](#)
- [27] J. Li, X. Li, X. Huang, R. Kaissner, F. Neubrech, S. Sun, and N. Liu. High space-bandwidth-product (sbp) hologram carriers toward photorealistic 3d holography. *Laser & Photonics Reviews*, 18(7):2301173, 2024. doi: 10.1002/lpor.202301173 [1, 2](#)
- [28] T. Liu, H. Ning, H. Cao, D. Luo, Z. Xu, C. Luo, G. Su, Y. Liu, R. Yao, and J. Peng. Research Progress of Large Viewing-Area 3D Holographic Near-Eye Display. *Laser & Photonics Reviews*, 18(4):2300641, 2024. doi: 10.1002/lpor.202300641 [1](#)
- [29] K. Matsushima. Rotational transformation for reconstruction of digital holography and egh creation. In *Adaptive Optics: Analysis and Methods-/Computational Optical Sensing and Imaging/Information Photonics/Signal Recovery and Synthesis Topical Meetings on CD-ROM*, p. 4, Sep 2007. doi: 10.1364/DH.2007.DWB4 [3](#)
- [30] K. Matsushima, H. Schimmel, and F. Wyrowski. Fast calculation method for optical diffraction on tilted planes by use of the angular spectrum of plane waves. *J. Opt. Soc. Am. A*, 20(9):1755–1762, Sep 2003. doi: 10.1364/JOSAA.20.001755 [3](#)
- [31] J.-H. Park and S.-B. Kim. Optical see-through holographic near-eye-display with eyebox steering and depth of field control. *Opt. Express*, 26(21):27076–27088, Oct 2018. doi: 10.1364/OE.26.027076 [1, 2](#)
- [32] Y. Peng, S. Choi, J. Kim, and G. Wetzstein. (2403-12) Speckle-free holography with partially coherent light sources and camera-in-the-loop calibration. *Science Advances*, 7(46):eabg5040, Nov. 2021. doi: 10.1126/sciadv.abg5040 [2](#)
- [33] Y. Peng, S. Choi, N. Padmanaban, and G. Wetzstein. Neural holography with camera-in-the-loop training. *ACM Trans. Graph.*, 39(6):185:1–185:14, Nov. 2020. doi: 10.1145/3414685.3417802 [2, 3, 6](#)
- [34] D. Pi, Y. Ye, K. Cheng, M. Gu, and X. Fang. Speckle-Free 3D Holography in the Wigner Domain. *Laser & Photonics Reviews*, p. 2401828, 2025. doi: 10.1002/lpor.202401828 [1](#)
- [35] L. Shi, B. Li, C. Kim, P. Kellnhofer, and W. Matusik. Towards real-time photorealistic 3d holography with deep neural networks! *Nature*, 591(7849):234–239, Mar. 2021. doi: 10.1038/s41586-020-03152-0 [2](#)
- [36] E. Tseng, T. Peng, and R. Horstmeyer. Neural Étendue expanders for high-throughput holography. *Nature Photonics*, 17(11):799–808, 2023. [9](#)
- [37] D. Wang, Z.-S. Li, Y.-W. Zheng, N.-N. Li, Y.-L. Li, and Q.-H. Wang. High-Quality Holographic 3D Display System Based on Virtual Splicing of Spatial Light Modulator. *ACS Photonics*, Dec. 2022. doi: 10.1021/acspophotonics.2c01514 [2](#)
- [38] X. Xia, F. Y. Guan, Y. Cai, and N. Magnenat Thalmann. Challenges and advancements for ar optical see-through near-eye displays: A review. *Frontiers in Virtual Reality*, 3, 2022. doi: 10.3389/fvrir.2022.838237 [1](#)
- [39] X. Xia, Y. Guan, A. State, P. Chakravarthula, T.-J. Cham, and H. Fuchs. Towards eyeglass-style holographic near-eye displays with statically expanded eyebox. In *2020 IEEE International Symposium on Mixed and Augmented Reality (ISMAR)*, pp. 312–319, 2020. doi: 10.1109/ISMAR50242.2020.00057 [9](#)
- [40] X. Xia, D. Ma, X. Meng, F. Qu, H. Zheng, Y. Yu, and Y. Peng. Off-axis holographic augmented reality displays with hoc-empowered and camera-calibrated propagation. *Photonics Research*, 13(3):687–697, 2025. [2](#)
- [41] X. Xia, W. Wang, F. Guan, F. Yang, X. Shui, H. Zheng, Y. Yu, and Y. Peng. Exploring angular-steering illumination-based eyebox expansion for holographic displays. *Opt. Express*, 31(19):31563–31573, Sept. 2023. doi: 10.1364/OE.498938 [1, 2](#)
- [42] H. Yeom, K. Hong, and M. Park. High-quality phase-only fourier hologram generation with camera-in-the-loop. *Optics Express*, 33:6615–6628, 2025. [9](#)
- [43] C. Yoo, M. Chae, S. Moon, and B. Lee. Retinal projection type lightguide-based near-eye display with switchable viewpoints. *Optics Express*, 28(3):3116–3135, Feb. 2020. doi: 10.1364/OE.383386 [2](#)
- [44] G. zhen Yang, B. zhen Dong, B. yuan Gu, J. yao Zhuang, and O. K. Ersoy. Gerchberg–saxton and yang–gu algorithms for phase retrieval in a nonunitary transform system: a comparison. *Appl. Opt., AO*, 33(2):209–218, Jan 1994. doi: 10.1364/AO.33.000209 [3](#)
- [45] W. Zhou, F. Qu, X. Meng, Z. Li, and Y. Peng. 3d-holonet: fast, unfiltered, 3d hologram generation with camera-calibrated network learning. *Optics Letters*, 50(4):1188–1191, 2025. [2, 9](#)